SUBMITTED TO THE ASTROPHYSICAL JOURNAL LETTERS
Preprint typeset using LaTeX style emulateapj v. 01/23/15

SIMULTANEOUS RADIO AND X-RAY OBSERVATIONS OF THE RADIO MAGNETAR SWIFT J1818.0−1607

KARISHMA BANSAL[1], AARON B. PEARLMAN[2,9,10], WALID A. MAJID[1,2], THOMAS A. PRINCE[2,1], GEORGE YOUNES[3,4], CHIN-PING HU[5,6], TERUAKI ENOTO[5],ROBERT S. WHARTON[1], JONATHAN KOCZ[2,7], AND SHINJI HORIUCHI[8]
[1] Jet Propulsion Laboratory, California Institute of Technology, Pasadena, CA 91109, USA; karishma.bansal@jpl.nasa.gov
[2] Division of Physics, Mathematics, and Astronomy, California Institute of Technology, Pasadena, CA 91125, USA
[3] Department of Physics, The George Washington University, Washington, DC 20052, USA
[4] Astronomy, Physics and Statistics Institute of Sciences (APSIS), The George Washington University, Washington, DC 20052, USA
[5] Extreme Natural Phenomena RIKEN Hakubi Research Team, RIKEN Cluster for Pioneering Research, 2-1 Hirosawa, Wako, Saitama 351-0198, Japan
[6] Department of Physics, National Changhua University of Education, Changhua 500, Taiwan
[7] Department of Astronomy, University of California, Berkeley, CA 94720, USA
[8] CSIRO Astronomy and Space Science, Canberra Deep Space Communications Complex, P.O. Box 1035, Tuggeranong, ACT 2901, Australia
Submitted to The Astrophysical Journal

ABSTRACT

Swift J1818.0−1607 is a recently discovered magnetar with a short spin period of 1.36 s and a magnetic field of $\sim 10^{14}$ Gauss. With an average estimated age of about 500 years, it is one of the youngest known isolated neutron stars with properties blurring the lines between high-B rotation-powered pulsars and magnetars. We have observed this source during multiple epochs, over a span of about six months, at high radio frequencies (S, X, and Ka bands) using the NASA Deep Space Network. In addition, we have observed it at two epochs in X-ray using the Neutron Star Interior Composition Explorer (NICER) telescope. We discover an anti-alignment (0.40 phase cycles) in the pulse profiles of its simultaneous radio and X-ray observations. We discuss different models to explain this large phase offset, which is likely due to the X-ray emission originating at the base of the hotspots and radio from the closed field lines. Moreover, we report its radio properties, such as a variation in the radio flux densities on the time scales of hours to months; a change from steep ($\alpha < -2.2$) to flat spectra ($\alpha = +0.3$) in about three weeks, followed by a spectral turnover at higher frequencies in a span of about three months, and the varying number of radio pulse profile components.

1. INTRODUCTION

Magnetars are neutron stars with large spin periods of $P = 2 - 12$ s and extreme magnetic fields ($B > 10^{14}$ G). So far about 30 magnetars have been detected, and most of them were detected in the X-ray from either the emission of energetic bursts or pulsed emission (Kaspi & Beloborodov 2017). Both of these emissions can be explained by the magnetar model (Duncan & Thompson 1992; Paczynski 1992). The persistent X-ray emission is expected from hotspots above the magnetic poles whereas, the X-ray bursts probably originate due to the large magnetic stress or the split and recombination of magnetic field lines. The luminosity of magnetar's persistent X-ray emission ranges between 10^{33} and 10^{35} erg s^{-1} (Thompson et al. 2002; Lyutikov 2003). Magnetars are highly variable, undergoing outburst episodes in conjunction with energetic short bursts, and during that time the number of photons increases. Based on their properties, these bursts can be divided into two main classes: giant flares (Palmer et al. 2005) and short X-ray bursts. Giant flares have an initial spike lasting a few milliseconds, followed by a minute-long exponentially decaying tail. These giant flares have a peak luminosity of $10^{44} - 10^{47}$ erg s^{-1} and are very rare with a rough occurrence of once per decade. Short X-ray bursts are the most common bursts and have a duration of about a few milliseconds to seconds, and a peak luminosity in the range of $10^{36} - 10^{43}$ erg s^{-1}.

Magnetars were believed to be radio-quiet until the first radio-emitting magnetar XTE J1810–197 was discovered (Camilo et al. 2006). In addition, four other radio magnetars, namely: PSR J1745–2900 (Eatough et al. 2013), PSR J1622–4950 (Levin et al. 2010), 1E 1547.0–5408 (Camilo et al. 2007a), and SGR 1935+2154 (Zhu et al. 2020), along with a transitional magnetar PSR J1119–6127 (Majid et al. 2017; Pearlman et al. 2019), have been discovered. Their properties, such as the flux density, change on the timescale of seconds to months, and the number of components in their profile may also change. Most of these magnetars shut down their emission for some period and typically re-emitting a burst in X-ray.

Swift Swift J1818.0−1607 is the sixth magnetar to exhibit radio emission. It was discovered on March 12, 2020, when the Burst Alert Telescope was triggered by a soft gamma-ray-burst (GCN 28055). Subsequent follow up observations in X-ray (Esposito et al. 2020) and radio (Champion et al. 2020) have found a spin period of 1.36 s and $\dot{P} = 8.160 \pm 2 \times 10^{-11}$ s s^{-1}, suggesting a magnetic field of 3.4×10^{14} G. Compared to typical magnetars, Swift J1818.0−1607 has one of the smallest spin periods, which is comparable to radio powered pulsars. Its profile has been found to be $80 - 100\%$ linearly polarized across a wide observing band (Lower et al. 2020). With an average characteristic age of 500 yr (Champion et al. 2020), it is the youngest known magnetars so far.

In this article, we compare the simultaneous radio and X-ray observations of Swift J1818.0−1607 using the NASA Deep Space Network (DSN; Pearlman et al. 2019) and the Neutron Star Interior Composition Explorer (NICER) telescope, respectively. We also study how the spectral properties of Swift J1818.0−1607's radio emission evolve over time. Based on these results, we draw comparisons of Swift J1818.0−1607 with other magnetars and typical radio pulsars. In Section 2.1 and 2.2, we describe our radio obser-

[9] NDSEG Research Fellow.
[10] NSF Graduate Research Fellow.

vations over six epochs and X-ray observations at two epochs. Then we discuss radio profile analysis in Section 3.1; radio spectral index in Section 3.2; our burst search in the X-ray data in Section 3.3; and X-ray profile in Section 3.4. We discuss these results and our implementations in Section 4 and summarize them in Section 5.

2. OBSERVATIONS

2.1. *Radio*

We carried out radio observations of Swift J1818.0−1607 during six epochs using different DSN radio telescopes (Table 1). The first two epochs (2020 March 15 and 2020 March 16) were carried out using DSS-35 and DSS-36, two 34 m diameter radio telescopes in Canberra, Australia. Subsequent observations on 2020 March 26, 2020, April 08, and 2020 July 15 (Epoch 3, 4, and 5) were carried out using DSS-63, a 70 m diameter radio telescope in Robledo, Spain. The most recent observation on 2020 August 10 (Epoch 6) was made using the DSS-35.

These observations were carried out in simultaneous dual frequency bands, in dual circular polarization mode, with center frequencies either at 2.2/8.4 GHz (S-band/X-band) or 8.4/32 GHz (X-band / Ka-band) as noted in Table 1. The usable bandwidth was roughly 110 MHz at S-band, 350 MHz at X-band, and 350 MHz at Ka-band. Data from both polarization channels in each frequency band were recorded in filterbank format containing channelized power spectral densities with the pulsar machines at each DSN complex, as described previously (e.g., Pearlman et al. 2018; Pearlman et al. 2019; Majid et al. 2020; Pearlman et al. 2020). The time and frequency resolution for Epochs 1, 2, and 6 were roughly 512 μs, and 1 MHz respectively. For epochs 3–5, the time and frequency resolution were roughly 2.2 ms and 0.46 MHz respectively. Additional information for each epoch, including the date and the starting time of each observing session, and its duration, are provided in Table 1.

The data processing procedures follow similar steps to those presented in previous studies of pulsars and magnetars with the DSN (e.g., Majid et al. 2017; Pearlman et al. 2018; Pearlman et al. 2019; Pearlman et al. 2020). Each data set was first corrected for bandpass slope across the frequency band. Subsequently, to remove low-frequency temporal variability, the moving average from each data value was subtracted using a 10 s window around each time sample. This was followed by the identification and masking of bad channels corrupted by radio frequency interference (RFI). The two polarization channels for each frequency band were then summed to form a total intensity time series. Each data set was then dedispersed at the nominal DM value of 706 pc cm^{-3} (Lower et al. 2020) and barycentered to the R.A. (J2000)= $18^h18^m0.12^s$ and Decl. (J2000)= $-16°07'52.80''$.

2.2. *X-ray*

X-ray observations of Swift J1818.0−1607 were carried out using the *NICER* X-ray Timing Instrument (XTI) (Gendreau et al. 2016), operating on the International Space Station. It operates in the soft X-ray energy range of $0.2 - 12$ keV with an effective area of 1900 cm^2 at 1.5 keV. It has absolute timing precision of < 300 ns. We observed Swift J1818.0−1607 on March 26, 2020 (Id: 3556011101), and April 04, 2020 (Id: 3556011801), for a duration of 2515 and 2890 seconds, respectively. These observations were part of the larger NICER program to monitor this source (Hu et al. 2020).

Initial data cleaning and reduction was carried using the Heasoft version 6.28 (HEASARC 2014). We filtered out the times with a high background count, near the South Atlantic Anomaly (SAA), when the angular separation was more than $0.015°$, and when the elevation angle was less than $30°$ above the limb of the Earth or less than $40°$ above the bright Earth limb. The events times were converted to barycenter time using the same coordinates as the radio observations (section 2.1) and the JPL DE405 solar system ephemeris.

3. RESULTS

3.1. *Radio Profiles*

We searched all datasets for evidence of pulsed emission near the spin period of the pulsar after dedispersing the data. No pulsed emission was detected on either 15 March (8.4/32 GHz) with DSS-35 or 16 March (2.2/8.4 GHz) with DSS-36. On 26 March, we observed with the 70-m dish DSS-63 at 2.2/8.4 GHz and detected pulsed emission at 2.2 GHz but not 8.4 GHz. On 08 April, we again detect Swift J1818.0−1607 at 2.2 GHz and make a marginal detection at 8.4 GHz. By 15 July, the magnetar is much brighter and very strong detections are made at both 2.2 and 8.4 GHz. With the magnetar apparently getting brighter at higher frequencies, we switched back to observing with the 34-m DSS-35 at 8.4 and 32 GHz on 10 August and made detections at both frequencies. The integrated and time-resolved pulse profiles all the detections are shown in Figure 1.

Like other radio-emitting magnetars, Swift J1818.0−1607 shows significant pulse profile evolution over time. At 2.2 GHz, the average pulse shape starts out fairly wide on 26 March with perhaps a trailing shoulder, then narrows by 08 April, before gaining a new leading component on 15 July. Similar pulse shape changes around the same time were also seen with the high cadence multi-frequency campaign of Champion et al. (2020), the 2.25/8.40 GHz observations of Huang et al. (2021), and the wideband $0.7 - 4$ GHz observations of Lower et al. (2021).

In addition to long-term evolution, we also see short-term variations in the form of mode switching. This is most prominent in the 15 July observations at 2.2/8.4 GHz. Figure 2 shows a side by side comparison of the pulse shapes at 2.2 and 8.4 GHz over the course of the observation. The dispersive delay has been removed, so the zero point of the phase is the same at each frequency. The profiles at both frequencies seem to switch between two modes. At 8.4 GHz, one mode is much brighter than the other, though the profile shapes are similar. At 2.2 GHz, the mode-switching occurs at exactly the same time as at 8.4 GHz. However, the pulse shape seems to change significantly from a single to double component profile. Huang et al. (2021) also report simultaneous mode switching at 2.25/8.40 GHz around the same time as our observations and moding at other frequencies has also been reported by others (Lower et al. 2021; Rajwade et al. 2022).

3.2. *Radio Flux Density and Spectral Index*

By simultaneously observing at two different frequency bands, our observations allow for simple spectral index measuremnts of Swift J1818.0−1607 in the months after its discovery. The period-averaged flux density measurements for all detections are given in Table 1. For non-detections, we set 7σ upper limits assuming a detection limit of

$$S_{\rm min} = \frac{({\rm S/N})_{\rm min}\, T_{\rm sys}}{G\sqrt{n_{\rm p}\Delta\nu T_{\rm obs}}}\sqrt{\frac{\delta}{1-\delta}} \qquad (1)$$

TABLE 1
RADIO OBSERVATIONS OF SWIFT SWIFT J1818.0−1607 WITH THE DSN

Epoch	Telescope	Obs Frequency (GHz)	Date[a]	Time[a] (hh:mm:ss)	Date[b] (MJD)	Duration (hr)
1	DSS-35	8.4, 32	2020 Mar 15	21:14:60	58923.88541	0.7
2	DSS-36	2.2, 8.4	2020 Mar 16	23:00:01	58924.95833	1.9
3	DSS-63	2.2, 8.4	2020 Mar 26	08:29:60	58934.35417	2.1
4	DSS-63	2.2, 8.4	2020 Apr 08	07:37:54	58947.31799	1.9
5	DSS-63	2.2, 8.4	2020 Jul 15	19:46:38	59045.82405	2.1
6	DSS-35	8.4, 32	2020 Aug 10	10:30:00	59071.43750	1.6

NOTE. — Parameters for the six dual-frequency observations.
[a] Start date and time of the observation (UTC).
[b] Start day of the observation (UTC).

TABLE 2
ROTATIONAL PERIOD AND FLUX DENSITY MEASUREMENT OF SWIFT SWIFT J1818.0−1607

Epoch	F0 (Hz)	S(2.2 GHz) (mJy)	S(8.4 GHz) (mJy)	S(32 GHz) (mJy)	Spectral Index
1	–	–	< 0.05	< 0.08	–
2	–	< 0.05	< 0.03	–	–
3	0.7333684(2)	0.80(2)	< 0.03	–	< -2.2
4	0.73335175(6)	0.31(6)	0.026(5)	–	$-1.9(2)$
5	0.7331469(2)	0.70(1)	1.00(2)	–	$+0.3(2)$
6	0.73309715(8)	–	0.7(1)	0.41(8)	$-0.4(2)$

NOTE. — Measured period averaged flux density of Swift J1818.0−1607 at each observing epoch. When no pulsations were detected we report a 7σ upper limit. Spectral indices are measured between the two frequencies observed. In the event that there is no detection at one of the frequencies we report a $x\sigma$ limit.

where $(\mathrm{S/N})_{\mathrm{min}} = 7$ is our detection threshold, T_{sys} and G are the system temperature and gain of the telescope, $n_{\mathrm{p}} = 2$ is the number of polarizations summed, $\delta\nu$ is the frequency bandwidth, T_{obs} is the observing time, and $\delta = W/P = 0.1$ is the assumed duty cycle of the pulsar. For epochs in which detections are made at both frequencies, we can measure a spectral index assuming the flux density follows a power-law form of $S_\nu \propto \nu^\alpha$. For epochs with one detection and one limit, we set a 7σ limit. The spectral indices and limits are given in Table 1.

Figure 3 shows the spectral index evolution out to about 150 days after the initial X-ray discovery on 12 March 2020 (Esposito et al. 2020). After two non-detections on 15 and 16 March, our first detection of Swift J1818.0−1607 on 26 March had a very steep 2.4-8.4 GHz spectral index of $\alpha_{2-8} < -2.2$. By 08 April, the spectral had flattened to $\alpha_{2-8} = -1.9 \pm 0.2$, which is more in line with typical radio pulsar spectral indices (e.g., Maron et al. 2000). The spectral continued to flatten so that by 15 July the spectral index was actually slightly inverted at $\alpha_{2-8} = +0.3 \pm 0.2$. Interestingly, one component in the 2.4 GHz profile on 15 July (Figure 1c) has a steep spectrum and does not show up at 8.4 GHz, while the other is inverted and gets brighter at 8.4 GHz. This is consistent with the so-called magnetar and pulsar modes seen by Lower et al. (2021). Finally, on 10 August we measure the 8.4-32 GHz spectral index to be $\alpha_{8-32} = -0.4 \pm 0.2$. The general trend of spectral flattening is consistent with the initial detections of Champion et al. (2020) and corroborate the much longer term 2.25/8.60 GHz measurements of Huang et al. (2021).

3.3. *X-ray Bursts*

We carried out a search for X-ray bursts in both X-ray observations (see Section 2.2) using unbinned event times. We employ the technique of Bayesian blocks (Scargle et al. 2013) which obtains optimal bins for a given dataset. This is a robust technique as it does not depend on the sampling or bin size of a dataset and can detect local structures in highly variable datasets. The datasets are first divided into optimum segments (blocks) such that there is no overlap between them and all model parameters, such as event rate, are constant within each block. The boundaries where a statistical model undergoes an abrupt change are called edges. These edges are used to form optimal histograms which help in identifying local structures (Lin et al. 2013). This prior distribution of blocks (ncp_{prior}) is obtained using Equation 21 in Scargle et al. (2013), which depends on the number of events (N) and the false probability ($p0$). In this paper, we use an inbuilt Bayesian Block function from AstroPy, with $p0 = 0.05$.

In our first X-ray observation of Swift J1818.0−1607 the edges overlap with the good time intervals (GTIs) suggesting that there are no bursts during this observation. However, for the second X-ray observation, we note that the number of edges is more than the number GTIs. Upon a closer investigation, we find a block at MJD 58947.2201 with a sudden increase in the count rate in a short duration, suggesting a soft x-ray burst. The number of photons in this burst is 5 and its duration is 0.0013 s. Its width has been obtained from the size

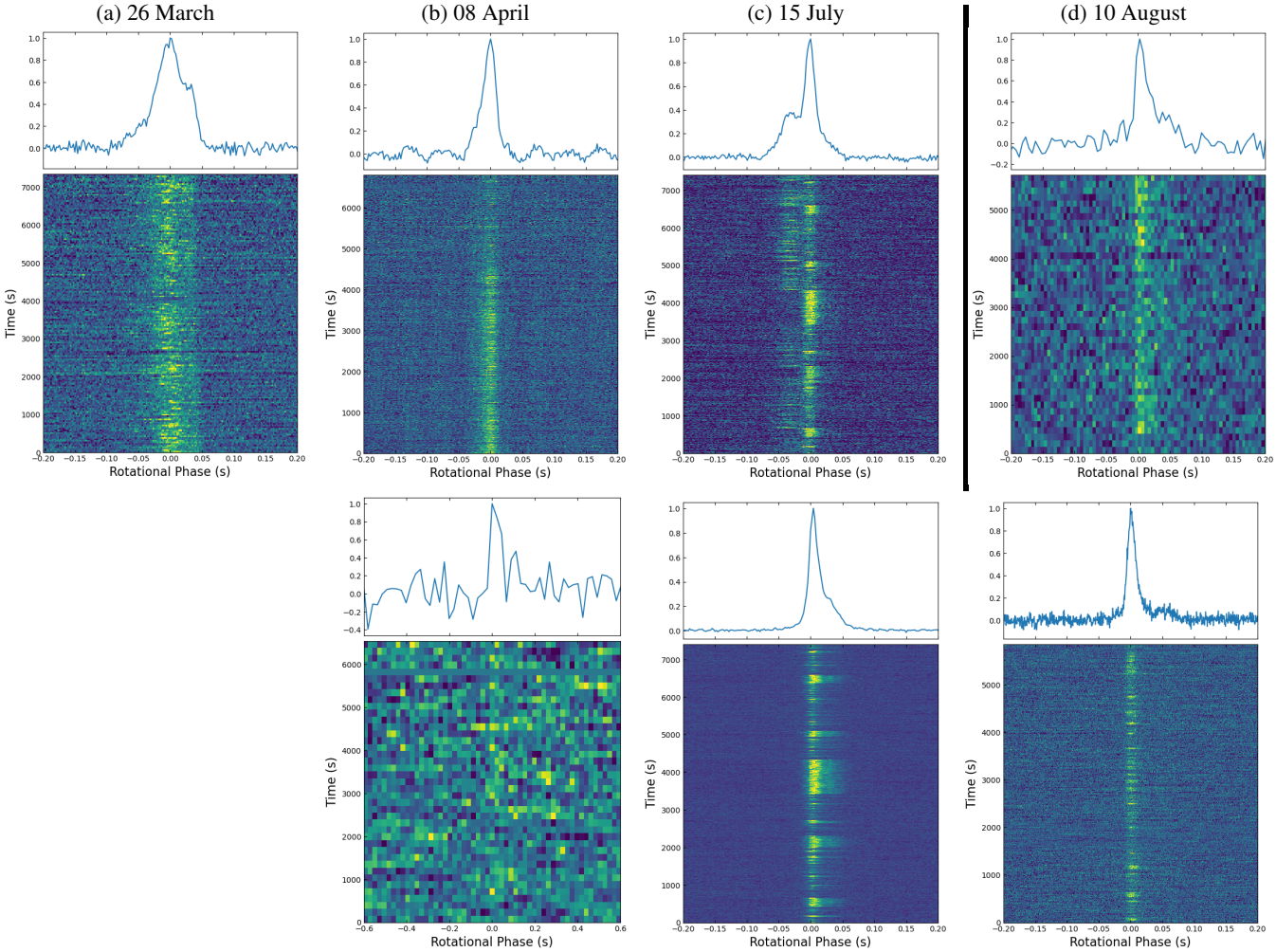

FIG. 1.— Folded radio profiles from the four observations with detections. The top row shows Swift J1818.0−1607 at 2.4 GHz (a-c) and 32 GHz (d), and the bottom row shows 8.4 GHz. Note that Swift J1818.0−1607 shows profile evolution on both long (days-months) and short (seconds-minutes) timescales. The short timescale changes on 15 Jully are the result of mode-switching (Figure 2) shows this in more detail.

of the representative Bayesian block. The mean count rate for this observation is 1.2 counts s^{-1}, which has been obtained from the spectral fitting in the energy range of 0.3–10 keV (Hu et al. 2020). For the duration of this burst, the mean count is 0.002. Assuming a Poisson distribution, we obtain the false alarm probability of this burst to be 2.7e-16. We have plotted the light curve of this burst in Figure 4. However, due to the low number of counts in this burst, we were unable to fit its spectrum.

3.4. *X-ray Profiles*

We obtain absolute X-ray phases for both epochs using PINT built-in functions (Luo et al. 2019), and the ephemeris obtained from contemporaneous radio analysis. We fold the X-ray data and obtain average X-ray profiles, one for each epoch. This is done using NICERSoft program [1], which uses the absolute phases, and filters out events with energies less than 2 keV and greater than 6 keV to select the most sensitive band of NICER telescope. In Figure 5, we plot the average X-ray pulse profiles (black) as well as the phaseogram for both epochs. Note that for Epoch 4 (Figure 5b), GTIs before and including the tentative X-ray burst have been excluded. The pulsed X-ray emission is consistent within the observation duration for each epoch, with no indication of any glitch. The RMS pulsed fraction (An et al. 2015) for Epoch 3 and Epoch 4 are 0.31 ± 0.02 and 0.36 ± 0.03, respectively. This increase in the pulsed fraction is consistent with those reported in Hu et al. (2020). We note that the X-ray pulse profile in the second observation has more structure as compared to that of the first one.

To investigate if there is any phase correlation between our simultaneous observations in radio and X-ray, we overlay the S-band average profiles (red) on X-ray profiles for both epochs. The location of the pulse peak in the X-ray profiles was obtained by fitting a sinusoidal function (blue). At both epochs, the peak of the radio pulse profile at S-band leads the X-ray pulse profile with a phase offset (in phase cycles) of 0.40 ± 0.03 and 0.33 ± 0.03, respectively. This offset implies that the peaks of radio and X-ray are almost misaligned with the radio occurring at X-ray pulse minimum. We validated this procedure by comparing the radio and X-ray profiles of the Crab pulsar. We confirmed that the peak of its radio profile at the S-band aligns with the peak of its X-ray profile, as expected (Hankins & Eilek 2007). We analyzed the recent NICER observation of Swift J1818.0−1607 in February 2021, to further test this phase misalignment, but no pulsed emission was detected in the X-ray.

4. DISCUSSION

4.1. *Radio Emission*

Swift J1818.0−1607 exhibits a range of radio profile changes in the 150 days after its initial X-ray discovery on 12 March 2020 (Esposito et al. 2020). The period-averaged flux density of the magnetar changes dramatically over the course of our observing campaign. After non-detections at 2.2, 8.4, and 32 GHz in the days after the X-ray discovery, we first detect Swift J1818.0−1607 at 2.2 GHz on 26 March 2020. The 2.2 GHz flux density of 0.8 mJy measured on 26 March means that the source got >16 brighter since the non-detection 10 days earlier. Similarly, the flux density of Swift J1818.0−1607 also increases dramatically at 8.4 and 32 GHz after the 2.2 GHz brightening, but gaps in our observations prevent us from determining exactly when this happened.

Although we did not detect Swift J1818.0−1607 on 15 or 16 March 2020, Champion et al. (2020) report detections at 1.5 GHz on both days with the Lovell Telescope and at 2.55 GHz on 15 March with the Effelsberg 100-m Telescope. This can mostly be attributed to the fact that we were using the smaller 34-m telescope during these observations and (on 15 March at least) at much higher frequencies. However, Swift J1818.0−1607 also showed extreme changes to flux density on day timescales in the first two weeks after discovery (Champion et al. 2020).

Since we observed simultaneously at two different frequency bands, we can directly measure the spectral index of Swift J1818.0−1607 over our observing campaign. In the first 150 days since the X-ray discovery, we find that the source gradually evolves from a very steep spectral index ($\alpha < -2.2$) to a much flatter spectral index ($\alpha \sim 0$) typically associated with radio magnetars. This spectral flattening confirms the initial indications from Champion et al. (2020) and is consistent with the high cadence dual-frequency 2.25/8.60 GHz observations of Huang et al. (2021) and the wideband $0.7 - 4.0$ GHz observations of Lower et al. (2021).

at 1.5 GHz. As the observing frequencies in Champion et al. (2020) are lower than our corresponding frequencies (Table 1), our non-detections are due to the steep spectrum of Swift J1818.0−1607 at these epochs. Similarly, there is a change in the spectral index of Swift J1818.0−1607between S-band and X-band as it goes from a steep spectrum of < -2.2 at Epoch 3 to a flat spectrum of $+0.3$ at Epoch 5, over a period of about three months. A similar variation in the spectral index (-0.97) has been reported in a recent observation of Swift J1818.0−1607 (Liu et al. 2020). In Epoch 6, we see a spectral turnover with an index of -0.4 between 8.4 GHz and 32 GHz, consistent with a recent estimate of -1.4 between 86 and 154 GHz (Torne et al. 2020).

The above characteristics of Swift J1818.0−1607 are analogous to other radio magnetars (Lazaridis et al. 2008; Torne et al. 2015). These variations could be intrinsic in origin, and maybe a result of frequency-dependent variability of the magnetar's intensity on short timescales, or due to the untwisting of magnetic field lines, which could also affect the pulse profile (Scholz et al. 2017). Swift J1818.0−1607 also shows a significant change in its pulse morphology at both 2.2 and 8.4 GHz over the span of our observations, similar to other radio magnetars such as XTE 1810-197 and SGR 1745-2900 (Camilo et al. 2007b; Pearlman et al. 2018). In addition, we also see a variation in the X-ray pulse profile as it becomes slightly more complex in Epoch 4 as compared to Epoch 3 (Figure 5). The flattening and high-frequency spectral turnover of Swift J1818.0−1607 spectra are accompanied by the emergence of secondary components as has been pointed out by Lower et al. (2021) and can also be seen in our observations at Epoch 5 and 6.

4.2. *X-ray Emission*

We search for X-ray bursts in our NICER observations of Swift J1818.0−1607 and detect one X-ray burst. In a recent study, Hu et al. (2020) reported additional 18 X-ray bursts from this source, detected using the NICER telescope. We also report the averaged X-ray pulsed emission from Swift J1818.0−1607 from two epochs in Figure 5. Thus, Swift J1818.0−1607 shows both persistent X-ray emission as

[1] https://github.com/paulray/NICERsoft

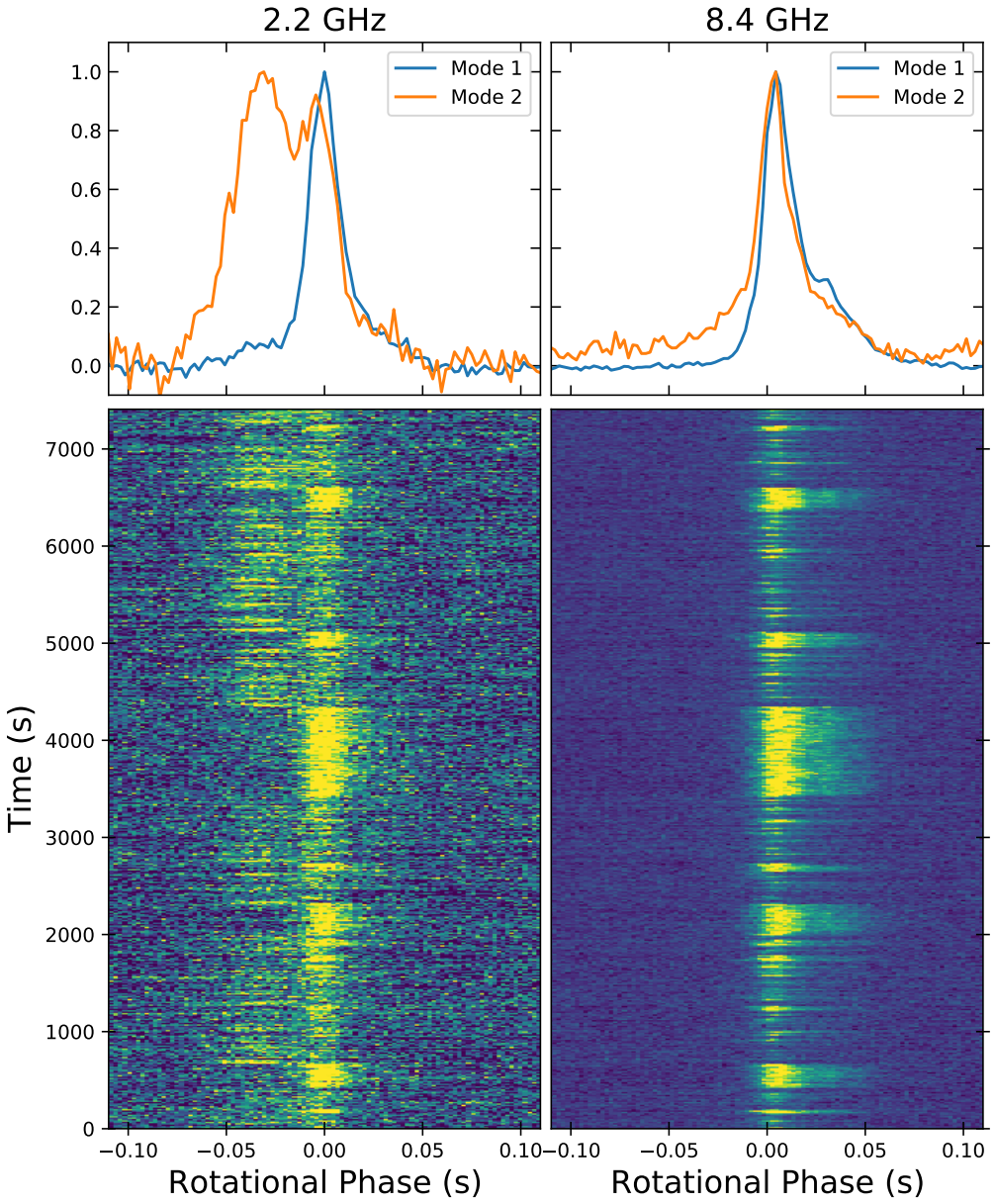

FIG. 2.— Mode switching in Swift J1818.0−1607 at 2.2 and 8.4 GHz on 15 July 2020. Each panel shows the changing pulse shape at both frequencies over the course of the observation. Mode 1 corresponds to the bright mode at 8.4 GHz and Mode 2 the fainter mode. The integrated pulse profiles from just the rotations in Mode 1 and Mode 2 are show in the top panels. In both cases Mode 1 is much brighter, but the profiles have been normalized so that the peak of each is the same.

well as a prolific number of X-ray bursts, a hallmark of magnetars.

4.3. *Radio and X-ray Alignment*

In the case of Swift J1818.0−1607 we find that radio and X-ray pulse profiles are misaligned (Figure 5) with a phase offset of $0.40(3)$ at Epoch 3 and $0.33(3)$ at Epoch 4 in phase cycles. A similar phase offset has been seen in another magnetar, such as XTE J1810-197, of about 0.11 ± 0.05 between the X-ray and radio observations (Pearlman et al. 2020). One possible way to obtain such phase offsets is due to thermal emission at X-ray and non-thermal emission at radio. A recent study (Hu et al. 2020) suggests that the X-ray emission in Swift J1818.0−1607 is likely thermal, as its spectrum is fit using a blackbody. This aligns with the theoretical prediction of the X-ray emission originating from the hotspots in the magnetars, which form as a result of charges in the open field lines (j-bundles) hitting the surface of the magnetar (Beloborodov 2009). The observed phase offset can be explained by the radio emission being caused by the closed magnetic field lines rather than the open j-bundles, which are much thicker. As Swift J1818.0−1607 is a relatively young source as compared to XTE J1810-197, it is likely to have a more twisted magnetosphere. This causes an inflated poloidal magnetic field, which shrinks as the magnetosphere untwists and the size of the hotspot reduces. This explains the observed increment in the pulsed fraction of Swift J1818.0−1607 over two epochs, suggesting a shrinkage in the size of polar hotspot (Hu et al. 2020).

Another possible explanation is the difference in the relative emission heights of X-ray and radio emission, which can also explain the change in linear position angle over time as noted by Lower et al. (2021). However, a phase offset of ~ 0.4 (phase cycles) in Swift J1818.0−1607 corresponds to the difference in emission heights of about 1.6×10^5 km which is about three times larger than its light-cylinder radius (6.5×10^4 km). This likely indicates that radio emission is likely not originating above the hotspot of the magnetar's surface. Moreover, the large polarization angle swing in Swift J1818.0−1607 was observed at only one epoch (Lower et al. 2021), which is not simultaneous with our observations, making it more difficult to draw any strong connection between them. Observations at both radio and X-ray, with simultaneous measurements of polarization angle, will enable us to determine the exact location of these emission regions in magnetars.

4.4. *Move to relevant sections*

The spectral index of Swift J1818.0−1607 shows a transition from steep to flat spectrum, unlike typical radio pulsars which have a stable steep spectral index of -1.8 ± 1 (Maron et al. 2000). In this aspect, it is similar to the transitional magnetar, PSR J1119-6127, which has also been found to emit X-ray bursts (Göğüş et al. 2016). However, similar to typical radio pulsars, both the spin period (0.33 s) and magnetic field (4.3×10^{13} Gauss) of PSR J1119-6127 are small as compared to Swift J1818.0−1607. The distinction between radio pulsars and magnetars arises due to the difference in their measured X-ray luminosities likely caused by a difference in underlying emission mechanisms. In radio pulsars, magnetic dipole radiation is the dominating emission process (Kramer 2009); however, in the case of magnetars, it is the decay of its strong internal magnetic field (Kaspi & Beloborodov 2017). So far, about 90 radio pulsars have been found to have X-ray emission (Becker 2009). Their properties vary depending on their characteristic age. Young pulsars, such as the Crab pulsar, are believed to emit non-thermal X-ray emission due to magnetospheric emission from charged particles, and their pulse profiles from both X-ray and radio align in phase (Becker 2009). Middle-aged pulsars, such as Vela, have been found to show thermal X-ray emission due to thermal cooling and heated polar caps. A few old non-recycled pulsars have been found to show both radio and X-ray emission, likely non-thermal, as their surface is not hot enough to produce thermal emission. For example, B1929+10 and B0950+08 are old pulsars, which exhibit both X-ray and radio emission, but their pulse profiles are anti-aligned (Becker et al. 2006). However, the exact reason for their misalignment is still unknown.

5. CONCLUSION

We study Swift J1818.0−1607 at multiple radio frequencies including the 32 GHz, over a span of about six months. We see a variation in its pulsed emission and flux density on the timescales of a few minutes to months. In addition, we note that Swift J1818.0−1607 shows a spectral turnover at higher frequencies, and has the largest change in the spectral index among other radio magnetars over a span of six months. These characteristics solidify its placement amongst the most intriguing radio-emitting magnetars, and an average estimated characteristic age of ~ 500 yrs further helps us in bridging the gap between magnetars and pulsars. Using our simultaneous X-ray and radio observations, we measure a large phase offset between their pulse profiles, which we attribute to the X-ray emission originating from the open field lines as opposed to the radio originating from the closed field lines. Future observations of this source will help us determine its true characteristic age, and measure how the phase offset between X-ray and radio pulse profiles evolves over time.

6. ACKNOWLEDGMENTS

A.B.P. acknowledges support by the Department of Defense (DoD) through the National Defense Science and Engineering Graduate (NDSEG) Fellowship Program and by the National Science Foundation (NSF) Graduate Research Fellowship under Grant No. DGE-1144469.

We thank the Jet Propulsion Laboratory's Spontaneous Concept Research and Technology Development program for supporting this work. We also thank Dr. Stephen Lichten for providing programmatic support. In addition, we are grateful to the DSN scheduling team (Hernan Diaz, George Martinez, and Carleen Ward) and the CDSCC and MDSCC operations staff for scheduling and carrying out these observations.

A portion of this research was performed at the Jet Propulsion Laboratory, California Institute of Technology and the Caltech campus, under a Research and Technology Development Grant through a contract with the National Aeronautics and Space Administration. U.S. government sponsorship is acknowledged.

REFERENCES

An, H., Archibald, R. F., Hascoët, R., et al. 2015, The Astrophysical Journal, 807, 93 [3.4]

Becker, W. 2009, X-Ray Emission from Pulsars and Neutron Stars (Berlin, Heidelberg: Springer Berlin Heidelberg), 91 [4.4]

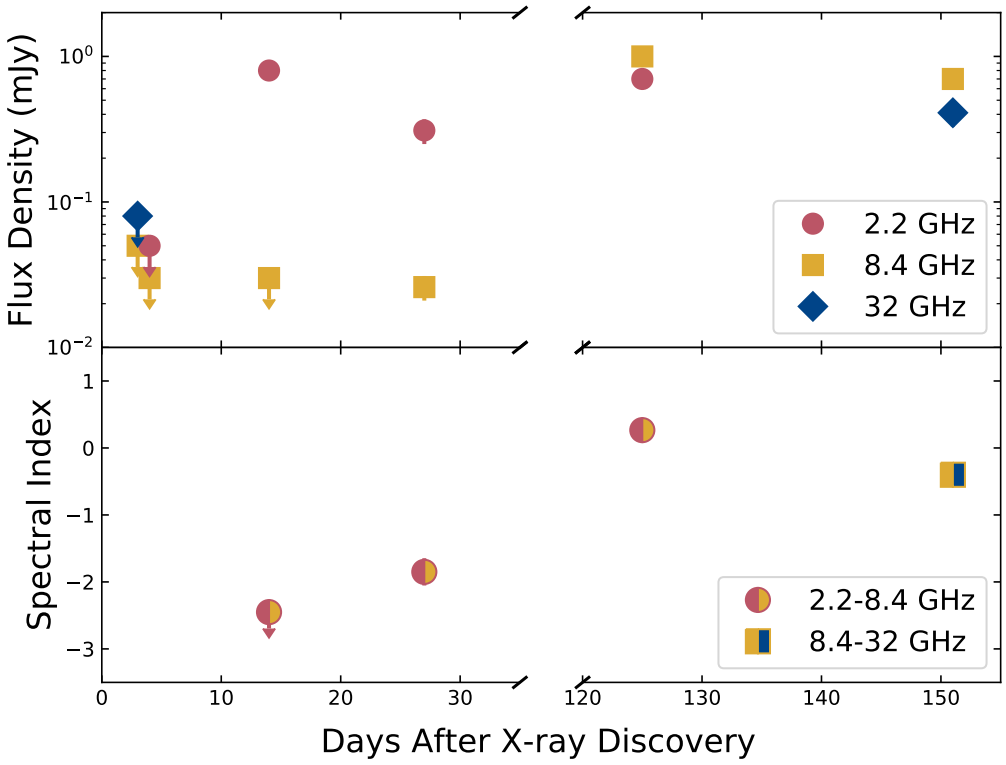

FIG. 3.— *Top:* Period-averaged flux density measurements of Swift J1818.0−1607 from dual band 2.2/8.4 GHz and 8.4/32 GHz observations. Non-detections show the 7σ upper limits. *Bottom:* Spectral indices derived from the dual-band observations.

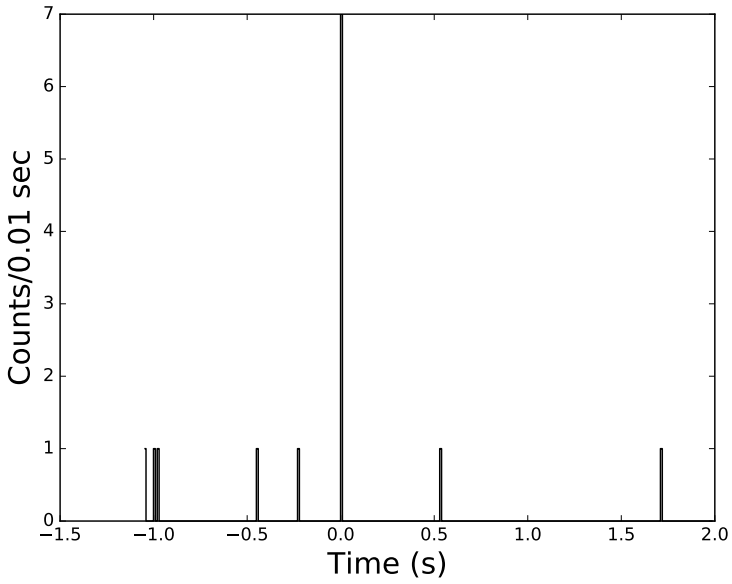

FIG. 4.— Light curve of a short X-ray burst in Swift J1818.0−1607 in the energy range 0.3-10 keV (Section 3.3). The number of photons in this burst are 5 and its width is 0.0015 s. It was observed using the NICER telescope with observation Id:3556011801.

Becker, W., Kramer, M., Jessner, A., et al. 2006, The Astrophysical Journal, 645, 1421 [4.4]
Beloborodov, A. M. 2009, ApJ, 703, 1044 [4.3]
Camilo, F., Ransom, S., Halpern, J., & Reynolds, J. 2007a, The Astrophysical Journal Letters, 666, L93 [1]
Camilo, F., Ransom, S. M., Halpern, J. P., et al. 2006, Nature, 442, 892 [1]
Camilo, F., Cognard, I., Ransom, S., et al. 2007b, The Astrophysical Journal, 663, 497 [4.1]
Champion, D., Cognard, I., Cruces, M., et al. 2020, Monthly Notices of the Royal Astronomical Society, 498, 6044–6056 [1, 3.1, 3.2, 4.1]
Duncan, R. C., & Thompson, C. 1992, ApJ, 392, L9 [1]
Eatough, R. P., Falcke, H., Karuppusamy, R., et al. 2013, Nature, 501, 391 [1]
Esposito, P., Rea, N., Borghese, A., et al. 2020, ApJ, 896, L30 [1, 3.2, 4.1]
Gendreau, K. C., Arzoumanian, Z., Adkins, P. W., et al. 2016, in Society of Photo-Optical Instrumentation Engineers (SPIE) Conference Series, Vol. 9905, Space Telescopes and Instrumentation 2016: Ultraviolet to Gamma Ray, 99051H [2.2]
Göğüş, E., Lin, L., Kaneko, Y., et al. 2016, The Astrophysical Journal, 829, L25 [4.4]
Hankins, T., & Eilek, J. 2007, The Astrophysical Journal, 670, 693 [3.4]
HEASARC, N. H. E. A. S. A. R. C. 2014, HEAsoft: Unified Release of FTOOLS and XANADU [2.2]
Hu, C.-P., Begicarslan, B., Guver, T., et al. 2020, NICER Observation of the Temporal and Spectral Evolution of Swift J1818.0-1607: a Missing Link between Magnetars and Rotation Powered Pulsars, arXiv:2009.00231 [astro-ph.HE] [2.2, 3.3, 3.4, 4.2, 4.3]
Huang, Z.-P., Yan, Z., Shen, Z.-Q., et al. 2021, MNRAS, 505, 1311 [3.1, 3.2, 4.1]
Kaspi, V. M., & Beloborodov, A. M. 2017, ARA&A, 55, 261 [1, 4.4]
Kramer, M. 2009, in IAU Symposium, Vol. 259, Cosmic Magnetic Fields: From Planets, to Stars and Galaxies, ed. K. G. Strassmeier, A. G. Kosovichev, & J. E. Beckman, 485 [4.4]
Lazaridis, K., Jessner, A., Kramer, M., et al. 2008, Monthly Notices of the Royal Astronomical Society, 390, 839 [4.1]
Levin, L., Bailes, M., Bates, S., et al. 2010, ApJ, 721, L33 [1]
Lin, L., Göğüş, E., Kaneko, Y., & Kouveliotou, C. 2013, ApJ, 778, 105 [3.3]
Liu, K., Karuppusamy, R., Cognard, I., et al. 2020, The Astronomer's Telegram, 13997, 1 [4.1]
Lower, M. E., Johnston, S., Shannon, R. M., Bailes, M., & Camilo, F. 2021, MNRAS, 502, 127 [3.1, 3.2, 4.1, 4.3]
Lower, M. E., Shannon, R. M., Johnston, S., & Bailes, M. 2020, ApJ, 896, L37 [1, 2.1]
Luo, J., Ransom, S., Demorest, P., et al. 2019, PINT: High-precision pulsar timing analysis package [3.4]
Lyutikov, M. 2003, MNRAS, 339, 623 [1]
Majid, W. A., Pearlman, A. B., Dobreva, T., et al. 2017, ApJ, 834, L2 [1, 2.1]
Majid, W. A., Pearlman, A. B., Nimmo, K., et al. 2020, ApJ, 897, L4 [2.1]
Maron, O., Kijak, J., Kramer, M., & Wielebinski, R. 2000, A&AS, 147, 195 [3.2, 4.4]
Paczynski, B. 1992, Acta Astron., 42, 145 [1]
Palmer, D. M., Barthelmy, S., Gehrels, N., et al. 2005, Nature, 434, 1107 [1]
Pearlman, A. B., Majid, W. A., & Prince, T. A. 2019, Advances in Astronomy, 2019, 6325183 [1, 2.1]
Pearlman, A. B., Majid, W. A., Prince, T. A., Kocz, J., & Horiuchi, S. 2018, The Astrophysical Journal, 866, 160 [2.1, 4.1]
Pearlman, A. B., Majid, W. A., Prince, T. A., et al. 2020, Bright X-ray and Radio Pulses from a Recently Reactivated Magnetar, arXiv:2005.08410 [astro-ph.HE] [2.1, 4.3]
Rajwade, K. M., Stappers, B. W., Lyne, A. G., et al. 2022, MNRAS, 512, 1687 [3.1]
Scargle, J. D., Norris, J. P., Jackson, B., & Chiang, J. 2013, ApJ, 764, 167 [3.3]
Scholz, P., Camilo, F., Sarkissian, J., et al. 2017, The Astrophysical Journal, 841, 126 [4.1]
Thompson, C., Lyutikov, M., & Kulkarni, S. R. 2002, ApJ, 574, 332 [1]
Torne, P., Eatough, R. P., Karuppusamy, R., et al. 2015, Monthly Notices of the Royal Astronomical Society: Letters, 451, L50 [4.1]
Torne, P., Liu, K., Cognard, I., et al. 2020, The Astronomer's Telegram, 14001, 1 [4.1]
Zhu, W., Wang, B., Zhou, D., et al. 2020, The Astronomer's Telegram, 14084, 1 [1]

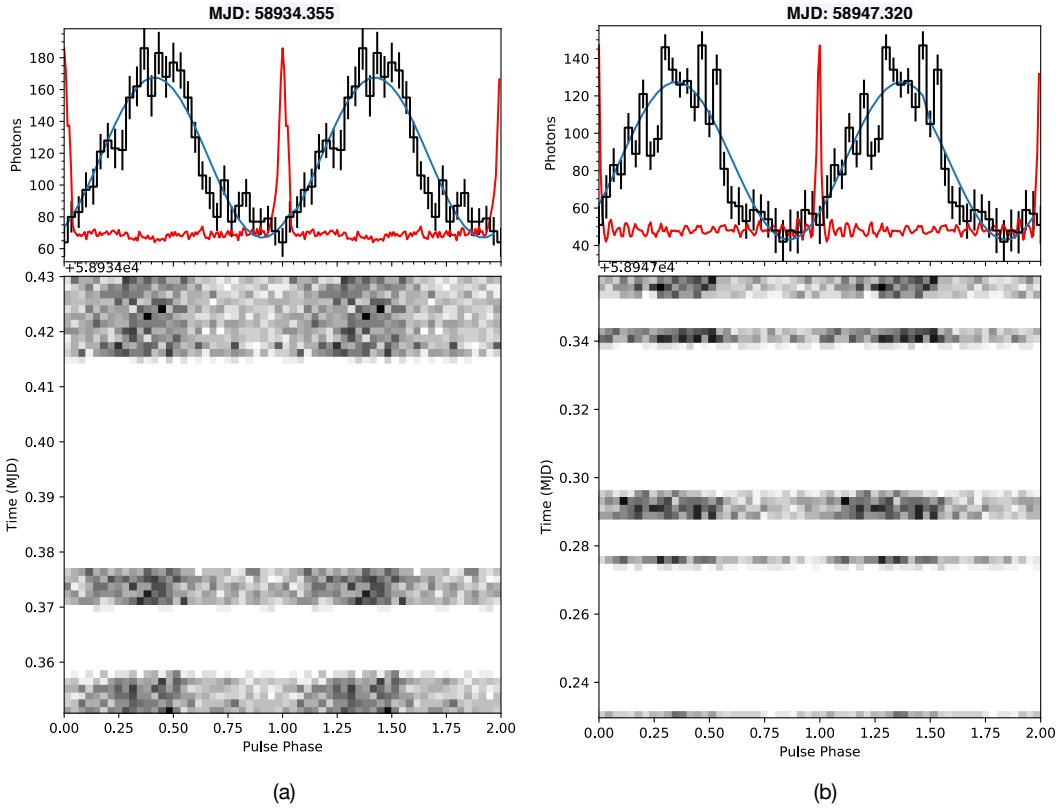

FIG. 5.— Integrated pulse profiles and phaseogram of Swift J1818.0−1607 at X-ray (black) during MJD 58934.35 (panel 1) and 58947.33 (panel 2). We fit each X-ray profile using a sinusoidal function (blue) and overlay the corresponding average pulse profile at S-band (red). The phase offset between radio and X-ray profile are 0.40 ± 0.03 (a) and 0.33 ± 0.03 (b).